A MATHEMATICAL INVESTIGATION OF THE ROLE OF INTRACRANIAL PRESSURE PULSATIONS AND SMALL GRADIENTS IN THE PATHOGENESIS OF HYDROCEPHALUS

KATHLEEN P. WILKIE, CORINA S. DRAPACA, AND SIVABAL SIVALOGANATHAN

Abstract. Cerebrospinal fluid (CSF) pulsations have been proposed as a possible causative mechanism for the ventricular enlargement that characterizes the neurological condition known as hydrocephalus. This paper summarizes recent work by the authors to anaylze the effect of CSF pulsations on brain tissue to determine if they are mechanically capable of enlarging the cerebral ventricles. First a poroelastic model is presented to analyze the interactions that occur between the fluid and porous solid constituents of brain tissue due to CSF pulsations. A viscoelastic model is then presented to analyze the effects of the fluid pulsations on the solid brain tissue. The combined results indicate that CSF pulsations in a healthy brain are incapable of causing tissue damage and thus the ventricular enlargement observed in hydrocephalus. Therefore they cannot be the primary cause of this condition. Finally, a hyper-viscoelastic model is presented and used to demonstrate that small long-term transmantle pressure gradients may be a possible cause of communicating hydrocephalus in infants.

Key words. Biomechanics, Hydrocephalus, Poroelasticity, Viscoelasticity, Fractional Calculus.

1. Introduction

Hydrocephalus is a condition characterized by the accumulation of cerebrospinal fluid (CSF) in the ventricles of the brain. Elevated intracranial pressure (ICP) and elevated intracranial pressure wave amplitudes are often observed in some manifestations of hydrocephalus. Non-communicating hydrocephalus occurs when a blockage in CSF flow causes an accumulation of fluid in the ventricles and an increase in ICP. In communicating hydrocephalus, where there is no blockage in CSF flow, large pressure gradients are not observed across the brain parenchyma. Thus, the standard explanation of how ventricles enlarge and why fluid accumulates no longer applies.

The relationship between intracranial pressure, intracranial compliance, and hydrocephalus is complex. Experimental evidence indicates that in hydrocephalus patients with a reduced compliance, the amplitude of ICP pulsations increases but then decreases back to normal upon shunt insertion [33, 38]. Other experiments demonstrate the synchrony between arterial and CSF pressure pulsations [20] and the effect these pulsations seemingly have on ventricular enlargement [3, 49].

Measurements of CSF pressure clearly indicate the pulsatile nature of CSF flow [26]. Some theories for the development of hydrocephalus postulate a link between these pulsations and ventricular enlargement [3, 28, 31, 49]. One such theory, proposed by Egnor et al. [11], suggests that the cranial compartment is in a natural state of resonance and that deviation from this state leads to a breakdown of the windkessel effect and a loss of normal cerebral blood and CSF dynamics. Intracranial pressure, however, is pulsatile in healthy brains and the frequency of these pulsations changes with the heart rate, leading one to ask "if CSF pulsations cause hydrocephalus, why don't we all have this condition?"

One possible mechanical explanation is that large amplitude CSF pulsations cause tissue damage in the periventricular regions of the brain. This hypothesis for the onset of hydrocephalus proceeds as follows. Each influx of arterial blood generates a CSF pressure pulse felt by the ventricle walls. Periodic pressurization of the walls causes the brain tissue to periodically compress and expand and CSF to oscillate in and out of the brain tissue. When these oscillations are large they generate large shear strains which damage the periventricular tissue. Finally, the damaged tissue allows fluid to penetrate further into the brain, propagating tissue damage and leading to ventricular expansion. We call this mechanistic theory the pulsation-damage hypothesis for hydrocephalus.

Mathematical models have been used to study hydrocephalus since the pioneering work of Hakim et al. [21, 22] in the 1970's, in order to further the understanding of how ventricular enlargement occurs and how treatments can be improved. In the literature, there are two main approaches to mathematically model hydrocephalus. The first approach uses time-dependent compartment models such as pressure volume models and analogous electrical circuit models [11, 12, 27, 37]. The second approach uses time- and space-dependent models such as poroelastic [29, 39, 40, 42, 43, 50] or viscoelastic [9, 10, 35, 36, 41, 46, 47] models. Both poroelastic and viscoelastic models are useful when modelling brain tissue and in this paper we will discuss the application of both classes of models to analyze the effect of CSF pulsations on brain tissue with regards to the development of hydrocephalus.

Biological tissues are composed of both fluid and solid phases and, in addition, the brain has 4 interconnected fluid compartments or ventricles through which the CSF circulates around the subarachnoid region of the brain and spinal cord areas. Thus, ventricular CSF pulsations affect the brain via the periodic loading and unloading of the ventricle walls and via the fluid exchange that occurs between the ventricular and interstitial spaces of the tissue. In Section 2 we present a poroelastic model and analyze the interactions that occur between the solid and fluid phases of brain tissue resulting from this fluid exchange. In Section 3 we present a viscoelastic model and analyze the effect of ventricular CSF pulsations on the solid brain. And in Section 4 we present a hyper-viscoelastic model and show that small long-term transmantle pressure gradients are capable of causing ventricular expansion in infants.

2. Brain Tissue as a Fluid-Solid Composite

We begin by presenting a poroelastic model to analyze the effects of periodic fluid exchange between the ventricles and the interstitial space of brain tissue resulting from CSF pulsations. The goal is to determine if the tissue strains and shear stresses produced in this way are sufficient to cause tissue damage and hence hydrocephalus.

2.1. Poroelastic Model Formulation. A simplified view of brain parenchyma is to think of the brain as a porous linearly elastic solid saturated in a viscous incompressible fluid. Such biphasic materials behave according to Biot's theory of consolidation [4]. Following the work of Tenti et al. [42] we assume a simple model geometry for which analytic solutions can be found. Thus, we model the brain as a thick walled cylinder: the interior representing the ventricles, the exterior representing the subarachnoid space (SAS) and skull, and the thick wall representing the brain parenchyma, see Figure 1. This tethered cylindrical geometry allows the assumption of planar strain and results in a simplification of the governing equations to one spatial dimension as a result of the radial symmetry.
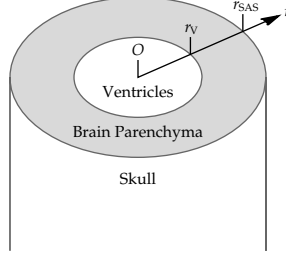
FIGURE 1.   Simplified cylindrical model geometry of the brain.

Applying conservation of momentum and Darcy's Law the poroelastic solid displacement, $\mathbf{u}$, satisfies the following equation of motion

$$(1) \qquad \rho\frac{\partial^2}{\partial t^2}\mathbf{u} = \frac{\mu}{k}\mathbf{W} + (\lambda + 2G)\nabla\left(\nabla\cdot\mathbf{u}\right) + G\nabla^2\mathbf{u},$$

where ρ is the density of the mixture, μ is the fluid viscosity, k is the solid porosity, and λ and G are the Lamé parameters of linear elasticity. In cylindrical coordinates, using symmetry, $\mathbf{u} = (u(r,t),0,0)$ and $\mathbf{W} = (W(r,t),0,0)$, where r is the radial position and t is time. The radial filtration velocity, $W(r,t)$, can be found by integrating the continuity equation, $\nabla\cdot(\mathbf{W} + \frac{\partial\mathbf{u}}{\partial t}) = 0$, which gives

$$W(r,t) = \frac{1}{r}c_0(t) - \frac{\partial}{\partial t}u(r,t),$$

where $c_0(t)$ is an arbitrary function of time. The pore pressure is assumed to have a static (constant) and a dynamic (time- and space-dependent) component, $p(r,t) = p_s + p_d(r,t)$. Darcy's Law relates the pore pressure to the solid displacement via the filtration velocity,

$$(2) \qquad \nabla p(r,t) = -\frac{\mu}{k}W(r,t) = -\frac{\mu}{k}\left(\frac{1}{r}c_0(t) - \frac{\partial}{\partial t}u(r,t)\right).$$

Writing equations (1) and (2) in cylindrical coordinates, we have two coupled partial differential equations (PDEs) for the solid displacement and the dynamic pore pressure:

$$(3) \qquad \frac{\partial^2 u}{\partial t^2} + f_r\frac{\partial u}{\partial t} = f_r\frac{1}{r}c_0(t) + c_d{}^2\left(\frac{\partial^2 u}{\partial r^2} + \frac{1}{r}\frac{\partial u}{\partial r} - \frac{1}{r^2}u\right)$$

$$(4) \qquad \frac{\partial p_d}{\partial r} = \frac{\mu}{k}\left(\frac{\partial u}{\partial t} - \frac{1}{r}c_0(t)\right),$$

where $f_r = \frac{\mu}{\rho k}$ is the relaxation frequency and $c_d = \sqrt{\frac{\lambda+2G}{\rho}}$ is the propagation speed of the dilatational waves.

Boundary conditions are required to determine the arbitrary constants that arise in the solutions to PDEs (3) and (4). For dynamic pore pressure, we require the amplitude of the pressure pulsations at the ventricle boundary ($r = r_V$) to match the amplitude of the ventricular CSF pulsations (p_V) and the amplitude of the pressure pulsations at the SAS boundary ($r = r_{SAS}$) to match the amplitude of the SAS CSF pulsations (p_{SAS}). That is, we require

$$(5) \qquad \begin{cases} p_d(r_V,t) = \mathrm{Re}\left(p_V\mathrm{e}^{i\omega t}\right) \\ p_d(r_{SAS},t) = \mathrm{Re}\left(p_{SAS}\mathrm{e}^{i\omega t}\right). \end{cases}$$

Since the parenchyma effectively sits in a fluid filled container, there should be no contact stress in the poroelastic solid at the ventricular and SAS boundaries. Thus we require

(6)
$$\begin{cases} (\lambda + 2G)\frac{\partial}{\partial r}u(r_V, t) + \frac{\lambda}{r_V}u(r_V, t) = 0 \\ (\lambda + 2G)\frac{\partial}{\partial r}u(r_{SAS}, t) + \frac{\lambda}{r_{SAS}}u(r_{SAS}, t) = 0. \end{cases}$$

To solve equations (3) and (4) we assume time harmonic motion, such that $u(r,t) = \mathrm{Re}\left(U(r)\mathrm{e}^{i\omega t}\right)$, $p_d(r,t) = \mathrm{Re}\left(P(r)\mathrm{e}^{i\omega t}\right)$, and $c_0(t) = \mathrm{Re}\left(C_0\mathrm{e}^{i\omega t}\right)$, where ω is the angular frequency of the pulsations. Substituting these into the PDEs and solving (see [45] for details) gives $U(r)$ and $P(r)$ as

(7)
$$U\left(\xi(r)\right) = -\frac{1}{c_d\alpha\xi}C_0 + \frac{c_d}{f_r}\left(C_1 J_1(\xi) + C_2 Y_1(\xi)\right),$$

(8)
$$P\left(\xi(r)\right) = -\frac{\omega^2\mu\ln(\frac{1}{\alpha}\xi)}{kf_r^2\alpha^2}C_0 - \frac{i\omega\mu c_d^2}{kf_r^2\alpha}\left(C_1 J_0(\xi) + C_2 Y_0(\xi)\right) + \mu f_r C_3,$$

where $\alpha = \sqrt{\frac{\omega^2}{f_r^2} - i\frac{\omega}{f_r}}$, $\xi(r) = \frac{\alpha f_r}{c_d}r$, and J_n and Y_n are the Bessel functions of order n. The constants C_0, C_1, C_2, and C_3 are determined by the boundary conditions and can be found by solving the matrix equation $\mathbb{A}\vec{x} = \vec{b}$, with vectors

$$\vec{x} = [\ C_0 \quad C_1 \quad C_2 \quad C_3\ ]^T, \quad \text{and} \quad \vec{b} = [\ p_V \quad p_{SAS} \quad 0 \quad 0\ ]^T,$$

and the matrix

$$\mathbb{A} = \begin{bmatrix} \frac{-\omega^2\mu\ln(\frac{\xi_V}{\alpha})}{kf_r^2\alpha^2} & \frac{-i\omega\mu c_d^2}{\alpha kf_r^2}J_0^V & \frac{-i\omega\mu c_d^2}{\alpha kf_r^2}Y_0^V & \mu f_r \\ \frac{-\omega^2\mu\ln(\frac{\xi_{SAS}}{\alpha})}{kf_r^2\alpha^2} & \frac{-i\omega\mu c_d^2}{\alpha kf_r^2}J_0^{SAS} & \frac{-i\omega\mu c_d^2}{\alpha kf_r^2}Y_0^{SAS} & \mu f_r \\ \frac{f_r}{\alpha c_d^2\xi_V} & \frac{M\xi_V}{2G}J_0^V - J_1^V & \frac{M\xi_V}{2G}Y_0^V - Y_1^V & 0 \\ \frac{f_r}{\alpha c_d^2\xi_{SAS}} & \frac{M\xi_{SAS}}{2G}J_0^{SAS} - J_1^{SAS} & \frac{M\xi_{SAS}}{2G}Y_0^{SAS} - Y_1^{SAS} & 0 \end{bmatrix},$$

where $M = (\lambda + 2G)$, $\xi_V = \frac{\alpha f_r}{c_d}r_V$, $\xi_{SAS} = \frac{\alpha f_r}{c_d}r_{SAS}$, and the notation $\mathcal{F}_n^B = \mathcal{F}_n(\frac{\alpha f_r}{c_d}r_B)$ with $n = 0$ or 1, $B = V$ or SAS, and $\mathcal{F} = J$ or Y, has been used for convenience. Finally, the filtration velocity is given by

(9)
$$W(r,t) = \frac{1}{r}\mathrm{Re}\left(C_0\mathrm{e}^{i\omega t}\right) - \mathrm{Re}\left(i\omega U(r)\mathrm{e}^{i\omega t}\right).$$

2.2. Poroelastic Model Simulations and Results. Eide [14] reported that in 6 out of 7 hydrocephalus patients studied, ICP measurements from the lateral ventricle and the brain parenchyma were synchronous but the amplitude of the ventricular pressure was significantly elevated compared to the parenchyma pressure. The smallest difference in the average peak-to-peak amplitude was 0.4 mm Hg with the other differences being 0.5, 1.0, and 2.6 mm Hg. For our numerical simulations, we choose the smallest measured difference (0.4 mm Hg) since larger differences would only scale the results proportionally. Furthermore, in patients without active hydrocephalus, no significant difference in ICP amplitude was found between the lateral ventricles and the brain parenchyma [5]. To prescribe the boundary condition at the subarachnoid space, we choose the same pressure wave amplitude as was measured in the parenchyma. This is justified by experimental measurements [13] showing no significant difference in wave amplitude between the pressures of the parenchyma and epidural space.

To simulate the conditions present in a normal pressure hydrocephalic brain, we define the average ventricular pressure to be 13 mm Hg, the ventricular pulse peak-to-peak amplitude to be 9.4 mm Hg, and the SAS pulse peak-to-peak amplitude to be 9.0 mm Hg. Other model parameter values have been taken from the literature, see Table 1. Note that the Lamé constants have been replaced by the more physical Young's modulus (E) and Poisson ratio (ν) via the standard relationships.

TABLE 1. Poroelastic model parameter values.

$\mu = 10^{-3}$ Kg m^{-1}s^{-1}	$\rho = 10^3$ Kg m^{-3}	$k = 10^{-14}$ m^2 [23]
$E = 21$ kPa [42]	$\nu = 0.4$ [42]	$\omega = 6$ rad s^{-1}
$p_V = \frac{1}{2}9.4$ mm Hg	$p_{SAS} = \frac{1}{2}9.0$ mm Hg	$p_s = 13$ mm Hg
$r_V = 3$ cm	$r_{SAS} = 10$ cm	$r_m = 6.5$ cm

In order to numerically simulate the analytic solutions found above, asymptotic expansions for the Bessel functions with large arguments [1] were used (see [45, Appendix A] for details). The model simulated pressure at the ventricle boundary, the SAS boundary, and in the middle of the parenchyma ($r = r_m$) is shown in Figure 2. The maximum pressure at the ventricular boundary is 17.7 mm Hg, at the SAS boundary it is 17.5 mm Hg, and in the middle of the parenchyma it is 17.48 mm Hg. Figure 2 matches the experimental observations [13, 14] in that a small dynamic pressure gradient exists across the ventricle wall into the parenchyma and that no significant pressure difference exists between the parenchyma and the SAS.
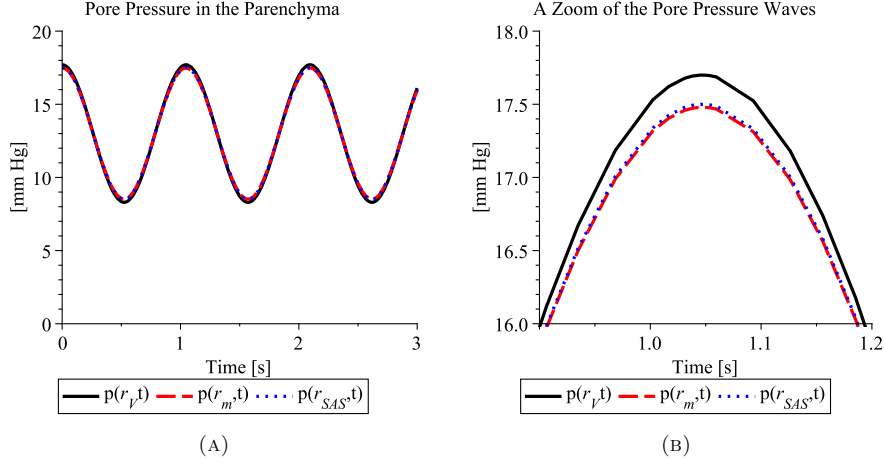

FIGURE 2. Simulated pressure waves at the boundaries (A), and a zoom showing the curve separations during systole (B).

In systole, the pressure is largest in the ventricle which causes an outward displacement of the parenchyma. The situation is reversed in diastole, and there is an inward displacement of the parenchyma. This oscillatory displacement is largest near the ventricle, with a maximum amplitude of 58.8 μm compared to the maximum displacement amplitude in the middle of the parenchyma 27.2 μm, or the SAS boundary 17.7 μm.

The pressure pulsations combined with the resulting compression and expansion cycle of the parenchyma cause the filtration of fluid in and out of the parenchyma at both boundaries as well as pulsations in fluid filtration all throughout the parenchyma. The filtration velocity is phase shifted from the displacement and pressure waves due to the conflict between the pressure gradient and the compressing parenchyma. The highest filtration velocities occur near the ventricle wall with a maximum magnitude of 1.08 μm/s.

2.3. Pore Flow Analysis. To determine if this shear-inducing pore flow is sufficient to damage tissue, we use a simple pipe flow model. By assuming the fluid is Newtonian, incompressible, and steady, and by neglecting body forces, the Navier-Stokes equations simplify to the following equation for flow through a straight pore,

$$(10) \qquad \nabla q = \mu \nabla^2 v,$$

where ∇q is the constant pressure gradient across the length of the pore, μ is the fluid viscosity, and v is the fluid flow along the pore. In a cylindrical pore $v = v(r)$, and the flow is given by

$$(11) \qquad v(r) = \frac{\nabla q}{4\mu}(r^2 - R^2),$$

where R is the radius of the pore and the following boundary conditions are imposed, $v(R) = 0$ and $\frac{dv}{dr}|_{r=0} = 0$.

Since the fluid flow through the porous material is governed by both the pressure gradient and the compression or expansion of the material, the pressure gradient used in this pore flow model, ∇q, is different from the pressure gradient in the poroelastic model. Thus, to determine the pressure gradient ∇q, we require the maximum velocity through the pore to be 1 μm/s. This provides an over approximation of the pressure gradient, $\nabla q = -1.6$ Pa, assuming a 100 μm diameter pore. The flow through the pore is thus given by

$$(12) \qquad v(r) = 400(R^2 - r^2),$$

where the viscosity of water, $\mu = 10^{-3}$ Pa·s, is assumed. Finally, the shear stress induced on the walls of the pore by a steady flow with a maximum velocity of 1 μm/s is given by

$$(13) \qquad \sigma = \mu \frac{dv}{dr}\bigg|_{r=R} = -40 \ \mu\text{Pa}.$$

Cells adhere to the extracellular matrix through the binding of integrin receptors to components such as fibronectin or collagen. Measurements of cell adhesion strength using shear flows in microfluidic channels average about 84 ± 27 Pa for cells adhered to low concentration collagen- or fibronectin-coated substrates [6]. The smallest observed adhesion strength was about 30 Pa and the largest observed strength was about 210 Pa. This is the force required to completely remove a cell from the substrate. Dong and Lei [8] estimated the force required to rupture one adhesive bond, or to extract a receptor from the cell membrane, as 1 μdyn (or 10^{-11} N). To estimate the shear, we assume this force is distributed over the top half of a cell attached to the pore wall. This provides a lower bound to the shear generated by this force acting directly on the smaller area of an integrin binding site. Assuming a spherical cell of radius 5 μm (the soma of a neuron ranges from 4 to 100 μm in diameter), this force corresponds to a surface shear of about 0.06 Pa. The estimated shear stress imposed by the fluid flow in the periventricular region

was about 40 μPa, which is three orders of magnitude smaller than the estimated stress required to break a single adhesive bond.

The maximum filtration velocity at the ventricle wall increases linearly with the pressure wave amplitude difference between the ventricles and SAS, $\Delta p = p_V - p_{SAS}$. The corresponding shear stress imposed on the wall of a cylindrical pore of radius 50 μm by this filtration also increases linearly with Δp. For a large pressure wave amplitude difference, $\Delta p = 2$ mm Hg (4 mm Hg peak-to-peak), the maximum pore velocity in the periventricular area is about 11 μm/s and the resulting shear force is about 450 μPa. This shear force is two orders of magnitude smaller than the estimated shear required to rupture a single adhesive bond. We conclude that trans-parenchymal fluid flow in response to CSF pulsations induces small shearing forces when compared to the forces required to induce tissue damage. Thus fluid flow through brain tissue is an unlikely contributor to tissue damage leaving only the internal solid stresses as a possible mechanism for damage in the pulsation-damage hypothesis of hydrocephalus.

3. Brain Tissue as a Viscoelastic Solid

Since we have excluded the interstitial fluid-solid interactions as a possible contributor to tissue damage, we may neglect the fluid phase of the tissue and consider brain tissue as a single-phase incompressible viscoelastic solid. Here we examine the effect of the periodic loading applied to the brain by ventricular CSF pulsations and estimate the ability of these pulsations to induce tissue damage and thus initiate hydrocephalus.

3.1. Fractional Zener Model Formulation. The fractional Zener viscoelastic model has recently been shown to predict the mechanical behaviour of biological tissues better than other viscoelastic models [7]. Using fractional derivatives in viscoelastic models introduces a history dependence into the constitutive equation, enabling accurate prediction of complex behaviour with relatively small numbers of model parameters. The fractional derivative of order α is defined by

$$D^\alpha f(t) = \frac{1}{\Gamma(1-\alpha)} \frac{\mathrm{d}}{\mathrm{d}t} \int_0^t (t-s)^{-\alpha} f(s)\,\mathrm{d}s,$$

where Γ is the Eulerian gamma function. The schematic of the Zener viscoelastic model is given in Figure 3. Here, σ is the stress, ϵ is the strain, E_1 and E_2 are the spring constants (elastic moduli) and μ is the viscosity of the dashpot.
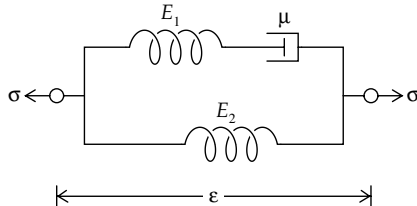

FIGURE 3. Schematic of the Zener viscoelastic model.

By defining an initial elastic modulus $E_0 = E_1 + E_2$, a steady-state elastic modulus $E_\infty = E_2$, and a relaxation time $\tau = \frac{\mu}{E_1}$, the constitutive equation for the fractional Zener model can be written as [7, 46]

(14) $$\sigma + \tau^\alpha D^\alpha \sigma = E_\infty \epsilon + E_0 \tau^\alpha D^\alpha \epsilon.$$

For simplicity, we assume the brain geometry to be a thick-walled cylinder, as in Figure 1, but with inner radius $r = a$ and outer radius $r = b$. Assuming the deviatoric behaviour of brain tissue can be modelled by the fractional Zener model and the dilatational behaviour can be modelled by the linear elastic model, the displacement of the parenchyma, a homogeneous, incompressible, isotropic solid, can be found analytically using the elastic-viscoelastic correspondence principle, see [46] for details. Because the skull plates are unfused in a newborn infant but fused in an adult, the boundary conditions must differ for the two cases of hydrocephalus. The boundary value problem for infant hydrocephalus prescribes zero radial stress at the skull boundary which allows for the large deformations observed in untreated cases,

$$(15) \qquad \text{Infant} \begin{cases} \frac{\partial}{\partial r}\sigma_{rr} + \frac{1}{r}(\sigma_{rr} - \sigma_{\theta\theta}) = 0 \\ \sigma_{rr} = -p_i(t) & \text{at } r = a \\ \sigma_{rr} = 0 & \text{at } r = b. \end{cases}$$

Meanwhile, in the case of adult hydrocephalus, zero displacement (u) is enforced at the outer boundary due to the rigidity of the mature skull, resulting in the boundary value problem

$$(16) \qquad \text{Adult} \begin{cases} \frac{\partial}{\partial r}\sigma_{rr} + \frac{1}{r}(\sigma_{rr} - \sigma_{\theta\theta}) = 0 \\ \sigma_{rr} = -p_i(t) & \text{at } r = a \\ u = 0 & \text{at } r = b. \end{cases}$$

Inertial forces are neglected by these models since the equilibrium equations are solved subject to the applied boundary conditions in order to determine the long-time effects of CSF pulsations on brain parenchyma. We assume a pulsatile pressure difference (ventricular pressure - SAS pressure) of the form $p_i(t) = p^* \cos(\omega t)$. More details on the model derivation and solution method can be found in [46]. The infant and adult displacement solutions to boundary value problems (15) and (16), u_I and u_A respectively, are [46, equations (12) and (19)]:

$$
\begin{aligned}
(17) \qquad u_I(r,t) = &\frac{a^2}{b^2 - a^2}\left[\left(\frac{3r}{6K + E_0} + \frac{b^2}{E_0 r} \right) p_i(t) \right. \\
&+ \frac{b^2(E_0 - E_\infty)}{E_0^2 \tau^\alpha r} p_i(t) * \left(t^{\alpha-1} E_{\alpha,\alpha}\left(-\frac{E_\infty}{E_0}\left(\frac{t}{\tau}\right)^\alpha \right) \right) \\
&+ \left. \frac{3r(E_0 - E_\infty)}{(6K + E_0)^2 \tau^\alpha} p_i(t) * \left(t^{\alpha-1} E_{\alpha,\alpha}\left(-\frac{6K + E_\infty}{6K + E_0}\left(\frac{t}{\tau}\right)^\alpha \right) \right) \right]
\end{aligned}
$$

and

$$
\begin{aligned}
(18) \quad u_A(r,t) = &\left(\frac{b}{r} - \frac{r}{b} \right)\left[\frac{3a^2 b}{(6K + E_0)a^2 + 3E_0 b^2} p_i(t) \right. \\
&+ \left. \frac{3a^2 b(a^2 + 3b^2)(E_0 - E_\infty)}{\left((6K + E_0)a^2 + 3E_0 b^2\right)^2 \tau^\alpha} p_i(t) * \left(t^{\alpha-1} E_{\alpha,\alpha}\left(-\hat{h}\left(\frac{t}{\tau}\right)^\alpha \right) \right) \right],
\end{aligned}
$$

where K is the bulk modulus, $E_{\alpha,\alpha}(z)$ is the generalized Mittag-Leffler function, $\hat{h} = \frac{(6K + E_\infty)a^2 + 3E_\infty b^2}{(6K + E_0)a^2 + 3E_0 b^2}$, and $*$ denotes the convolution operation over time.

3.2. Viscoelastic Model Simulations and Results. The tissue displacements predicted in [46] used the fractional Zener model parameter values found by Davis et al. [7] by fitting the model to the relaxation data of Galford and McElhaney [17] (see the Davis et al. parameter values in Table 2). An amplitude of 667 Pa (10 mm Hg peak-to-peak) was chosen to recreate the large pressure pulses observed during the

induction of hydrocephalus [30] as well as during hydrocephalus with increased intracranial pressure [14]. The frequency is based on a heart rate of 70 beats per minute. See the common parameter values listed in Table 2 for the rest of the model parameters. Algorithms for the numerical computation of the generalized Mittag-Leffler function can be found in [18, 19].

The maximum displacement amplitude of the ventricle wall predicted by the model with these parameter values was 3 mm in the infant case and 48 nm in the adult case [46]. The maximum solid stresses were 670 Pa (radial) and 800 Pa (tangential) for the infant case and 670 Pa (both radial and tangential) for the adult case. These predictions were compared to the predictions of the standard viscoelastic model [36] by Wilkie *et al.* [46].

3.2.1. Age-Dependent Parameters. Since the brain undergoes an incredible growth spurt as it matures and develops over the first two years of life, it is reasonable to assume that the material properties also change over this time. To determine how the fractional Zener model parameter values compare for infant and adult brain tissue, and how these different material properties may affect the above predictions, we use the age-dependent shear complex modulus porcine data reported by Thibault and Margulies [44]. Using the nonlinear least squares method `lsqcurvefit` in `MATLAB`, the fractional Zener model parameter values were estimated [47] by fitting the shear complex modulus for the fractional Zener model $(G^*(i\omega) = G'(\omega) + iG''(\omega))$, with

$$(19) \qquad G'(\omega) = \frac{E_\infty + (E_0 + E_\infty)\tau^\alpha\omega^\alpha \cos\left(\frac{\alpha\pi}{2}\right) + E_0\tau^{2\alpha}\omega^{2\alpha}}{1 + 2\tau^\alpha\omega^\alpha \cos\left(\frac{\alpha\pi}{2}\right) + \tau^{2\alpha}\omega^{2\alpha}},$$

and

$$(20) \qquad G''(\omega) = \frac{(E_0 - E_\infty)\tau^\alpha\omega^\alpha \sin\left(\frac{\alpha\pi}{2}\right)}{1 + 2\tau^\alpha\omega^\alpha \cos\left(\frac{\alpha\pi}{2}\right) + \tau^{2\alpha}\omega^{2\alpha}},$$

to the porcine data [44]. The results of this data fitting give the fractional Zener model parameter values for infant and adult brain tissue listed in Table 2.

TABLE 2. Fractional Zener model parameter values.

Davis et al. Parameter Values [7]			
$E_\infty = 1612$ Pa $\quad E_0 = 7715$ Pa	$\tau = 6.7009$ s	$\alpha = 0.641$	
Infant Parameter Values [47]			
$E_\infty = 621$ Pa $\quad E_0 = 6678$ Pa	$\tau = 110$ μs	$\alpha = 0.779$	
Adult Parameter Values [47]			
$E_\infty = 955$ Pa $\quad E_0 = 96\,073$ Pa	$\tau = 6.92$ μs	$\alpha = 0.786$	
Common Parameter Values			
$a = 3$ cm $\qquad b = 10$ cm	$p^* = 667$ Pa	$K = 2.1$ GPa	$\omega = 7$ rad/s

Using these infant and adult parameter values for the fractional Zener model, the displacements of the parenchyma predicted by (17) and (18) are shown in Figure 4. The infant porcine parameter values predict unphysical displacements in our infant hydrocephalus model: the maximum displacement of the ventricle wall is 35 mm which is greater than the 30 mm inner radius of the model geometry. The

adult case predicts a maximum displacement of 48 nm, the same as was previously predicted [46] using the parameter values of Davis et al. [7].
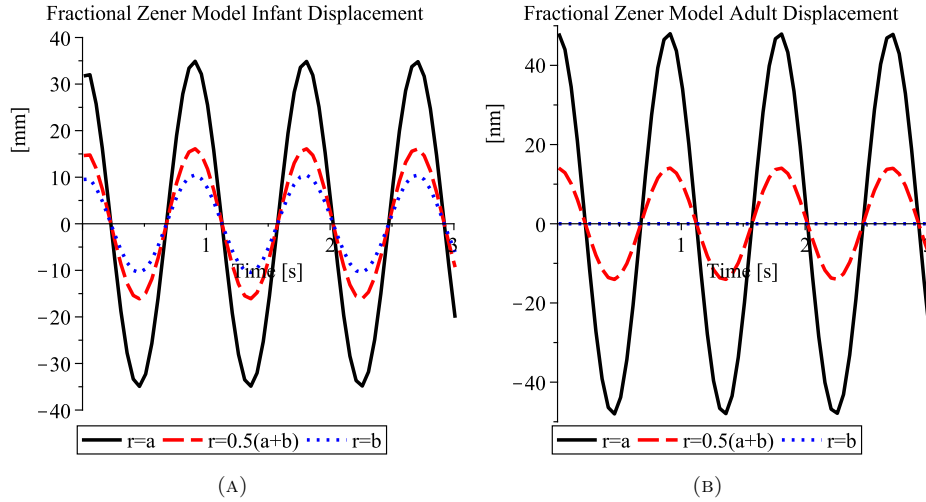

FIGURE 4. Parenchyma displacements for the (A) infant (in mm) and (B) adult (in nm) cases predicted by the fractional Zener model using the age-dependent parameter values in Table 2.

The unphysical result obtained in the infant case is due to either an unphysical mathematical model or poor experimental data. The model gives physical and reasonable predictions in the adult case but not in the infant case where smaller elastic moduli are used. It is possible that the zero stress boundary condition assigned in the infant case (15) is too weak. This condition was previously used [25, 34, 42, 46] to avoid the free boundary value problem. Assuming that the infant brain is enclosed in a thin elastic membrane representing the unfused skull, and that the large deformations observed in hydrocephalus occur over time scales much larger than those considered here, this boundary condition appears to be a reasonable approximation.

3.3. A Mixed Boundary Condition. An alternative boundary condition for the infant hydrocephalus case can be constructed from the adult case. The solution to the adult boundary value problem (16) gives an expression for the stress at the outer boundary ($r = b$), we call this stress $q(t)$. Assuming the infant skull provides a fraction, δ, of the restrictive force the adult skull provides, we can assign a new mixed boundary condition for the infant hydrocephalus case,

$$(21) \qquad \sigma_{rr} = \delta q(t) \quad \text{at } r = b.$$

From [46, equation (20)], the radial stress at $r = b$ in the adult hydrocephalus case is

$$(22) \quad q(t) = \frac{-(6K + 4E_0)a^2}{(E_0 + 6K)a^2 + 3E_0 b^2} \, p_i(t) - \frac{6K(E_\infty - E_0)\tau^{-\alpha}a^4}{((6K + E_0)a^2 + 3E_0 b^2)^2} \, p_i(t) * F(t)$$

where $F(t) = t^{\alpha-1}E_{\alpha,\alpha}\left(-\hat{h}\left(\frac{t}{\tau}\right)^\alpha\right)$.

Since the PDE in (15) is linear, boundary condition (21) corresponds to the linear combination of the two original boundary value problems, (15) and (16). That is, the brain tissue displacement solution of the mixed boundary value problem, u_m, is

$$(23) \qquad u_m(r,t) = (1-\delta)u_I(r,t) + \delta u_A(r,t),$$

where $0 \leq \delta \leq 1$, u_I is the infant displacement (17), and u_A is the adult displacement (18).

Since the unfused sutures of the infant skull are softer than the cranial bones, large internal pressures cause bulging of the sutures and fontanelles but negligible displacement of the cranial plates, indicating that the cranial plates are relatively fixed and rigid for short time scales. Over long time scales, however, a large internal pressure coupled with the normal growth processes of the brain will cause the skull to enlarge abnormally. In this work, where short time scales are analysed, we thus assume that the infant cranial bones are relatively rigid, and that when they are coupled with unfused sutures, the infant skull provides a fraction of the resistive force provided by the adult skull. Assuming this fraction to be about 50% ($\delta = 0.5$), the mixed boundary value problem predicts a maximum displacement at the ventricle wall of 17.5 mm. A more clinically common ventricular wall displacement, about 5 mm [24], requires a value of $\delta \approx 0.86$, implying that the infant skull provides about 86% of the resistive force provided by the adult skull.

The amplitude of the radial and tangential stresses in the infant and adult cases with age-appropriate parameter values range from 670 to 800 Pa [46] and the stresses for the mixed boundary value problem are of similar magnitudes [47]. Franceschini et al. [15] estimated the damage threshold for white matter to be 2.71 kPa. Even though the tissue stresses are largest in the periventricular region, the stress magnitudes reported here are 25% to 30% of this damage threshold. Thus, it seems unlikely that the increased amplitude of CSF pulsations and the resulting tissue displacements are singularly responsible for the tissue damage and ventricular expansion observed in hydrocephalus.

The infant cerebrum steady-state elastic modulus was determined to be about 600 Pa which is consistent with the value of 584 Pa previously proposed [41]. Interestingly, the storage and loss moduli of brain tissue were found to decrease with age in patients over the age of 18 years [32]. Thus, it is possible that the steady-state elastic modulus increases from the infant value of about 600 Pa to a maximum value of about 1000 Pa at early adulthood and then decreases with age. If this hypothesis is correct, then the increased occurrence of hydrocephalus in the infant and elderly populations may be partially explained by a reduced steady-state elastic modulus, which renders the tissue more susceptible to large deformations and to the development of hydrocephalus. This effect would be enhanced when coupled with a reduced bulk modulus in the elderly, which was previously conjectured [46].

4. An Alternate Hypothesis for Hydrocephalus

From the results of the previous two models, it seems reasonable to conclude that the CSF pulsations cannot be the primary cause of ventricular expansion in hydrocephalus due to their inability to induce shearing or internal stresses large enough to damage tissue. An alternate hypothesis for the pathogenesis of hydrocephalus is the absorption-degradation hypothesis which proposes that alternate pathways for CSF absorption occur within the brain tissue causing small intramantle and transmantle pressure gradients to occur. These essentially undetectable (1 mm Hg or less) pressure gradients coupled with degraded tissue properties may be the cause

of some cases of communicating hydrocephalus. Here, by focusing on the infant case with age-appropriate material parameters, we show that pressure gradients on the order of 1 mm Hg are large enough to cause ventricular expansion.

4.1. Fractional Kelvin-Voigt Model Formulation.

Encouraged once again by the success of fractional derivatives in viscoelastic models, we assume that the behaviour of brain tissue can be modelled as a fractional Kelvin-Voigt viscoelastic solid where a hyperelastic spring is coupled in parallel to a fractional viscoelastic dashpot. Using again the simplified cylindrical geometry of the brain, we denote the undeformed inner and outer radii as R_1 and R_2, respectively. For time $t > 0$, the cylinder is allowed to deform in response to the boundary conditions and the Eulerian cylindrical co-ordinate system (r, θ, z) deforms with the material. The inner boundary, r_1, represents the ventricle wall while the outer boundary, r_2, represents the cortical surface. Full details on the derivation of this model are presented in Wilkie et al. [48].

Boundary conditions are prescribed in terms of the radial stress, σ_r, and include $\sigma_r(t, r_1) = -p_0(t)$, where $p_0(t)$ is the pressure difference between the ventricles and the SAS, and $\sigma_r(t, r_2) = 0$, a stress-free outer surface. Hydrocephalus develops over a period of weeks, so we assume that $p_0(t)$ varies slowly and we neglect inertial forces. In response to the internal pressure, assuming the ends of the cylinder are tethered, radially symmetric deformations will occur. Thus $r = f(t, R)$, where R is the initial undeformed radius and f is the unknown deformation function.

Since brain tissue is nearly incompressible, the third principal invariant of the left Cauchy-Green deformation tensor must be unitary. Thus, the deformation function is $f(t, R) = \sqrt{R^2 + R_1^2 B(t)}$, where $B(t)$ is an unknown function of time. The Kelvin-Voigt viscoelastic model consists of a spring connected in parallel to a dashpot. We assume that the spring is a homogeneous, isotropic, hyperelastic material with a strain energy density function of the Mooney-Rivlin form, and that the viscous dashpot is fractional with order α, where $0 \leq \alpha \leq 1$.

Integrating and applying our boundary conditions to the equilibrium equation, obtained by considering the conservation of momentum, gives the following nonlinear integro-differential equation

$$p_0(t) = \frac{\mu}{2} \int_1^b \left(\frac{1}{x} - \frac{x}{\left(x + B(t)\right)^2} \right) \mathrm{d}x$$

(24)
$$+ \frac{\eta}{2\Gamma(1-\alpha)} \int_0^t \frac{\dot{B}(\tau)}{(t-\tau)^\alpha} \int_1^b \left(\frac{1}{\left(x + B(\tau)\right)^2} + \frac{1}{\left(x + B(t)\right)^2} \right) \mathrm{d}x \, \mathrm{d}\tau,$$

where μ is the shear modulus, η is the fractional viscosity, b is the nondimensional ratio $b = \left(\frac{R_2}{R_1} \right)^2$, $\Gamma(z)$ is the Eulerian Gamma function, and $\dot{B}(t) = \frac{\mathrm{d}B}{\mathrm{d}t}$. Assuming small strains, $(B(t) \ll 1)$, simplifies Equation 24 to a linear integro-differential equation with the Abel kernel,

(25)
$$\mu B(t) + \frac{\eta}{\Gamma(1-\alpha)} \int_0^t (t-\tau)^{-\alpha} \dot{B}(\tau) \, \mathrm{d}\tau = \frac{b}{b-1} p_0(t).$$

With an internal pressure of the form $p_0(t) = \delta p$, where δp is small enough to satisfy the assumption of small strains, the steady-state solution to Equation 25 is $B_{ss} = \frac{b}{b-1} \frac{\delta p}{\mu}$. Thus, the steady-state deformations of the ventricle wall (r_1) and

cortical surface (r_2) are

$$(26) \qquad r_k(t) = \sqrt{R_k^2 + R_1^2 \frac{b}{b-1} \frac{\delta p}{\mu}},$$

for $k = 1$, 2. The width of the deformed brain is $r_2(t) - r_1(t)$.

4.2. Hyper-Viscoelastic Model Simulations and Results. To estimate the steady-state finite deformation resulting from a pressure gradient on the order of 1 mm Hg, we apply an iterative numerical method based on an incremental law for soft biological tissues. As demonstrated by Fung [16, pg. 238–239, Fig. 7.7:1] with rabbit mesentery, small incremental loading-unloading curves can be used to approximate a finite strain loading-unloading curve. Using this concept, we divide a finite deformation-causing pressure gradient, $p_0(t) = \Delta p$, into n tiny increments, δp, with $n\delta p = \Delta p$, to approximate the finite deformation in an incremental manner.

For δp sufficiently small, the small strain steady-state solution to Equation 25 gives the slightly deformed description of the brain, Equation 26. Applying a second pressure increment, δp, and solving for the small strain solution with this already slightly deformed brain, gives an approximation to the deformation that results from a pressure gradient of magnitude $2\delta p$. The result of this second application of the incremental pressure, δp, is given by Equation 26 where R_1 and R_2 are updated to the previous values of r_1 and r_2 found after the first application of δp. Iterating this procedure n times approximates the finite deformation resulting from the pressure gradient Δp.

To simulate the steady-state behaviour of a newborn infant brain under the action of an internal pressure gradient, we define the undeformed boundaries to be $R_1 = 2$ cm and $R_2 = 6$ cm. The value of the steady-state shear modulus for infant brain tissue is $\mu \approx \frac{E_\infty}{3} \approx 200$ Pa [47] from the work discussed in Section 3.
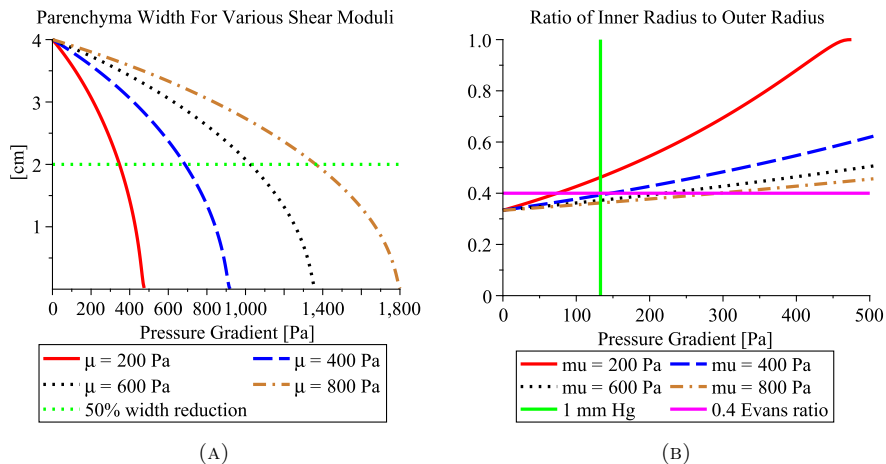

FIGURE 5. Incremental simulation of parenchyma width (A) and Evans ratio (B) as the total applied pressure gradient is increased in increments of 5 Pa. Note that 1 mm Hg = 133 Pa.

The reduction in brain tissue width is shown in Figure 5 for four values of the shear modulus and an incremental pressure gradient small enough to guarantee

small strains ($\delta p = 5$ Pa). With a total applied pressure gradient of 1 mm Hg ($\Delta p = 133$ Pa), the brain tissue width is reduced by 15% for $\mu = 200$ Pa (33% for $\mu = 100$ Pa, 10% for $\mu = 300$ Pa, and 8% for $\mu = 400$ Pa). A reduction by 50% occurs when the pressure gradient is about 350 Pa (2.6 mm Hg) for $\mu = 200$ Pa. The Evans ratio, a diagnostic tool for identifying hydrocephalus, is defined as the ratio of the maximal width of the frontal horns to the maximal width of the brain parenchyma. A ratio greater than 0.4 indicates a hydrocephalic brain. Figure 5B demonstrates that with our assumed initial configuration ($R_1 = 2$ cm, $R_2 = 6$ cm, and $\mu = 200$ Pa), the ratio of the inner radius to the outer radius (an approximation of the Evans ratio) crosses the 0.4 threshold with an applied pressure gradient of less than 1 mm Hg. These rough estimates suggest that hydrocephalus may develop under sustained pressure gradients on the order of 1 mm Hg, especially if developmental, microstructural or chemical changes within the tissue cause the mechanical properties (shear modulus) to be reduced, as is the case in the infant brain.

5. Discussion

From the analyses presented in Section 2 and Section 3 we conclude that the CSF pulsations induce insufficient shear stresses within the brain to mechanically damage tissue (both at the cellular and tissue levels), and thus, the pulsation-damage hypothesis should be revised. In particular, the ability of these oscillatory shearing forces to cause phenotypic changes in the brain tissue cells should be explored. Cellular level changes, such as a reduction in cell-matrix adhesion, will alter the mechanical properties of the tissue. These changes, when combined with other mechanisms such as abnormal osmotic pressures, have the potential to create the necessary conditions for ventricular expansion [2, 45]. In Section 4, the analysis suggests that in an infant brain, where the steady-state elastic modulus is reduced compared to adult brain tissue [47], long-term pressure gradients on the order of 1 mm Hg (essentially undetectable by clinical pressure sensors) are sufficient to enlarge the ventricles. This indicates that the absorption-degradation hypothesis may be plausible and should be explored further, especially as it relates to infant and elderly cases of communicating hydrocephalus where the mechanical properties of the brain may vary considerably from those of a young adult.

Acknowledgements

References

[1] M. Abramowitz and I. A. Stegun, editors. *Handbook of Mathematical Functions With Formulas, Graphs, and Mathematical Tables.* U.S. Government, 1972. http://www.math.sfu.ca/ cbm/aands/index.htm.

[2] R. Begg and K. Wilkie. A mechanism for ventricular expansion in communicating hydrocephalus. In *Proceedings of the OCCAM-Fields-MITACS Biomedical Problem Solving Workshop.* `http://www.math.uwaterloo.ca/~kpwilkie/OCCAM_Hydrocephalus_Report.pdf`, 2009.

[3] E. Bering. Circulation of the cerebrospinal fluid: Demonstration of the choroid plexuses as the generator of the force for flow of fluid and ventricular enlargement. *J. Neurosurg.*, 19:405–413, 1962.

[4] M. A. Biot. General theory of three-dimensional consolidation. *J. App. Phys.*, 12:155–164, February 1941.

[5] A. Brean, P. Eide, and A. Stubhaug. Comparison of intracranial pressure measured simultaneously within the brain parenchyma and cerebral ventricles. *J. Clin. Monit.Comput.*, 20(6):411–414, 2006.

[6] K. Christ, K. Williamson, K. Masters, and K. Turner. Measurement of single-cell adhesion strength using a microfluidic assay. *Biomed. Microdevices*, 12(3):443–455, June 2010.

[7] G. Davis, M. Kohandel, S. Sivaloganathan, and G. Tenti. The constitutive properties of the brain parenchyma part 2: Fractional derivative approach. *Med. Eng. Phys.*, 28:455–459, 2006.

[8] C. Dong and X. Lei. Biomechanics of cell rolling: Shear flow, cell-surface adhesion, and cell deformability. *J. Biomech.*, 33(1):35–43, 2000.

[9] C. Drapaca, G. Tenti, K. Rohlf, and S. Sivaloganathan. A quasilinear viscoelastic constitutive equation for the brain: Application to hydrocephalus. *J. Elast.*, 85(1):65–83, 2006.

[10] T. Dutta-Roy, A. Wittek, and K. Miller. Biomechanical modelling of normal pressure hydrocephalus. *J. Biomech.*, 41:2263–2271, 2008.

[11] M. Egnor, A. Rosiello, and L. Zheng. A model of intracranial pulsations. *Pediatr. Neurosurg.*, 35(6):284–298, 2001.

[12] M. Egnor, L. Zheng, A. Rosiello, F. Gutman, and R. Davis. A model of pulsations in communicating hydrocephalus. *Pediatr. Neurosurg.*, 36:281–303, 2002.

[13] P. K. Eide. Comparison of simultaneous continuous intracranial pressure (ICP) signals from ICP sensors placed within the brain parenchyma and the epidural space. *Med. Eng. Phys.*, pages 34–40, 2008.

[14] P. K. Eide. Demonstration of uneven distribution of intracranial pulsatility in hydrocephalus patients. *J. Neurosurg.*, 109(5):912–917, 2008.

[15] G. Franceschini, D. Bigoni, P. Regitnig, and G. Holzapfel. Brain tissue deforms similarly to filled elastomers and follows consolidation theory. *J. Mech. Phys. Solids*, 54:2592–2620, 2006.

[16] Y.-C. Fung. *Biomechanics: Mechanical Properties of Living Tissues*. Springer-Verlag New York Inc., 1981.

[17] J. Galford and J. McElhaney. A viscoelastic study of scalp, brain and dura. *J. Biomech.*, 3:211–221, 1970.

[18] R. Gorenflo, J. Loutchko, and Y. Luchko. Computation of the Mittag-Leffler function $E_{\alpha,\beta}(z)$ and its derivative. *Fract. Calc. Appl. Anal.*, 5(4):491–518, 2002.

[19] R. Gorenflo, J. Loutchko, and Y. Luchko. Corrections to the paper "computation of the Mittag-Leffler function $E_{\alpha,\beta}(z)$ and its derivative". *Fract. Calc. Appl. Anal.*, 6(1):111–112, 2003.

[20] D. Greitz. Cerebrospinal fluid circulation and associated intracranial dynamics - a radiologic investigation using MR imaging and radionuclide cisternography. *Acta Radiologica Suppl.*, 386:1–23, 1993.

[21] S. Hakim. Biomechanics of hydrocephalus. *Acta Neurol. Latinoamer.*, 17:169–174, 1971.

[22] S. Hakim, J. Venegas, and J. Burton. The physics of the cranial cavity, hydrocephalus and normal pressure hydrocephalus: Mechanical interpretation and mathematical model. *Surg. Neurol.*, 5:187–210, 1976.

[23] M. Kaczmarek, R. Subramaniam, and S. Neff. The hydromechanics of hydrocephalus: steady-state solutions for cylindrical geometry. *Bull. Math. Biol.*, 59(2):295–323, 1997.

[24] E. Lee, J. Wang, and R. Mezrich. Variation of lateral ventricular volume during the cardiac cycle observed by mr imaging. *Am. J. Neuroradiol.*, 10:1145–1149, 1989.

[25] D. Levine. The pathogenesis of normal pressure hydrocephalus: A theoretical analysis. *Bull. Math. Biol.*, 61:875–916, 1999.

[26] A. A. Linninger, C. Tsakiris, D. C. Zhu, M. Xenos, P. Roycewicz, Z. Danziger, and R. Penn. Pulsatile cerebrospinal fluid dynamics in the human brain. *IEEE Trans. Biomed. Eng.*, 52(4):557–565, 2005.

[27] A. Marmarou, K. Shulman, and R. Rosende. A nonlinear analysis of the cerebrospinal fluid system and intracranial pressure dynamics. *J. Neurosurg.*, 48:332–344, 1978.

[28] T. Milhorat. Choroid plexus and cerebrospinal fluid production. *Science*, 166:1514–1516, 1969.

[29] T. Nagashima, N. Tamaki, S. Matsumoto, B. Horwitz, and Y. Seguchi. Biomechanics of hydrocephalus: a new theoretical model. *Neurosurg.*, 21(6):898–904, 1987.

[30] R. D. Penn, M. C. Lee, A. A. Linninger, K. Miesel, S. N. Lu, and L. Stylos. Pressure gradients in the brain in an experimental model of hydrocephalus. *J. Neurosurg.*, 102:1069–1075, 2005.

[31] C. D. Rocco, G. D. Trapani, V. Pettorossi, and M. Caldarelli. On the pathology of experimental hydrocephalus induced by artificial increase in endoventricular CSF pulse pressure. *Child's Brain*, 5(2):81–95, 1979.

[32] I. Sack, B. Beierbach, J. Wuerfel, D. Klatt, U. Hamhaber, S. Papazoglou, P. Martus, and J. Braun. The impact of aging and gender on brain viscoelasticity. *NeuroImage*, 46:652–657, 2009.

[33] J. Seibert, T. McCowan, W. Chadduck, J. Adametz, C. Glasier, S. Williamson, B. Taylor, R. J. Leithiser, J. McConnell, C. Stansell, and et al. Duplex pulsed doppler US versus intracranial pressure in the neonate: Clinical and experimental studies. *Radiology*, 171(1):155–159, 1989.

[34] S. Sivaloganathan, M. Stastna, G. Tenti, and J. Drake. Biomechanics of the brain: A theoretical and numberical study of Biot's equations of consolidation theory with deformation-dependent permeability. *Int. J. Non Linear Mech.*, 40:1149–1159, 2005.

[35] S. Sivaloganathan, M. Stastna, G. Tenti, and J. Drake. A viscoelastic approach to the modelling of hydrocephalus. *Appl. Math. Comput.*, 163:1097–1107, 2005.

[36] S. Sivaloganathan, M. Stastna, G. Tenti, and J. Drake. A viscoelastic model of the brain parenchyma with pulsatile ventricular pressure. *Appl. Math. Comput.*, 165:687–698, 2005.

[37] S. Sivaloganathan, G. Tenti, and J. Drake. Mathematical pressure volume models of the cerebrospinal fluid. *Appl. Math. Comput.*, 94:243–266, 1998.

[38] F. H. Sklar and M. Linder. The role of the pressure-volume relationship of brain elasticity in the mechanics and treatment of hydrocephalus. In K. Shapiro, A. Marmarou, and H. Portnoy, editors, *Hydrocephalus*, pages 323–336. Raven Press, 1984.

[39] A. Smillie, I. Sobey, and Z. Molnar. A hydroelastic model of hydrocephalus. *J. Fluid Mech.*, 539:417–443, 2005.

[40] I. Sobey and B. Wirth. Effect of non-linear permeability in a spherically symmetric model of hydrocephalus. *Math. Med. Biol.*, 23(4):339–361, 2006.

[41] Z. Taylor and K. Miller. Reassessment of brain elasticity for analysis of biomechanisms of hydrocephalus. *J. Biomech.*, 37:1263–1269, 2004.

[42] G. Tenti, S. Sivaloganathan, and J. Drake. Brain biomechanics: Steady-state consolidation theory of hydrocephalus. *Can. App. Math. Q.*, 7(1):111–124, 1999.

[43] G. Tenti, S. Sivaloganathan, and J. Drake. Mathematical modeling of the brain: Principles and challenges. *Neurosurg.*, 62(5):1146–1157, 2008.

[44] K. L. Thibault and S. S. Margulies. Age-dependent material properties of the porcine cerebrum: effect on pediatric inertial head injury criteria. *J. Biomech.*, 31:1119–1126, 1998.

[45] K. Wilkie. *Cerebrospinal fluid pulsations and aging effects in mathematical models of hydrocephalus.* PhD thesis, University of Waterloo, 2010.

[46] K. Wilkie, C. Drapaca, and S. Sivaloganathan. A theoretical study of the effect of intraventricular pulsations on the pathogenesis of hydrocephalus. *Appl. Math. Comput.*, 215:3181–3191, 2010.

[47] K. Wilkie, C. Drapaca, and S. Sivaloganathan. Aging impact on brain biomechanics with applications to hydrocephalus. *Math. Med. Biol.*, 2011. doi: 10.1093/imammb/dqr001.

[48] K. Wilkie, C. Drapaca, and S. Sivaloganathan. A nonlinear viscoelastic fractional derivative model of infant hydrocephalus. *Appl. Math. Comput.*, 217:8693–8704, 2011.

[49] C. Wilson and V. Bertan. Interruption of the anterior choroidal artery in experimental hydrocephalus. *Arch. Neurol.*, 17(6):614–619, 1967.

[50] B. Wirth and I. Sobey. An axisymmetric and fully 3D poroelastic model for the evolution of hydrocephalus. *Math. Med. Biol.*, 23(4):363–388, December 2006.

Center of Cancer Systems Biology, St. Elizabeth's Medical Center, Tufts University School of Medicine, Boston, MA, USA

Department of Engineering Science and Mechanics, The Pennsylvania State University, University Park, PA, 16802, USA

Department of Applied Mathematics, University of Waterloo, Waterloo, ON, N2J 3G1, Canada
E-mail: `ssivalog@uwaterloo.ca`